The Role of Surface Hydroxyls in Dehydration and Dehydrogenation of Formic Acid on $Fe_3O_4(001)$

Marcus A. Sharp, Hoan K. K. Nguyen, Christopher J. Lee, Eric Sauter, Yuemin Wang, Christof Wöll, Benjamin A. Jackson, Mal-Soon Lee, Bruce D. Kay, Simone Raugei,* Líney Árnadóttir,* and Zdenek Dohnálek*

ABSTRACT: Understanding the role of surface structure and hydroxylation in catalytic reactions on metal oxide surfaces is important for developing a mechanistic insight into the complex interface processes. Here, we investigate the reactivity of formic acid on reconstructed $Fe_3O_4(001)$ using a combination of X-ray photoelectron spectroscopy, infrared reflection absorption spectroscopy, temperature-programmed reaction spectroscopy, low energy electron diffraction, and electronic structure calculations. We find that formic acid initially dissociates at low temperatures (<80 K) into bidentate formate and a hydroxyl up to an initial dosed coverage of two HCOOH per $Fe_3O_4(001)$ unit cell. At higher temperatures (>450 K), formate largely decomposes along the dehydration pathway, producing CO and H_2O, with dehydrogenation to CO_2 being a minority side reaction. As a first step, water formation leads to surface oxygen extraction via the Mars-van Krevelen mechanism. Computational studies reveal formate embedded in oxygen vacancies as a key intermediate in the CO formation mechanism. CO formation proceeds via two reaction pathways with desorption that peaks at 530 K on the hydroxyl-rich surface and 560 K on the hydroxyl-deficient surface. Atomic hydrogen coadsorption experiments and *ab initio* calculations reveal that the presence of surface hydroxyls reduces the CO formation barrier. These results highlight the complex interactions between substrate and intermediate species occurring during reactions on metal oxide surfaces.

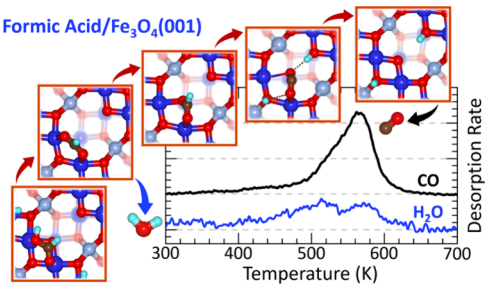

1. INTRODUCTION

Understanding the interactions of organic molecules with metal oxide surfaces is essential for developing an insight into processes occurring in a broad range of areas, such as corrosion, geochemistry, and catalysis. For catalysis, fundamental surface science studies are critical to advance our mechanistic understanding of chemical processes and reaction pathways on well-defined model surfaces. One such surface, the $(\sqrt{2} \times \sqrt{2})R45°$ reconstructed $Fe_3O_4(001)$, has gained significant interest due to its ability to stabilize single transition metal atoms at elevated temperatures.[1−9] In catalysis, magnetite is utilized as oxide support for the water−gas shift (WGS)[10−12] and Fischer−Tropsch[13−16] reactions. In the WGS reaction, formate ($HCOO^-$) is considered an important intermediate, while formic acid (HCOOH) is a desirable product of carbon dioxide (CO_2) hydrogenation reactions.[12,17−19] As such, studies of formic acid conversion on magnetite Fe_3O_4 surfaces are of fundamental interest for characterizing the mechanisms, energetics, and kinetics of elementary reaction steps on bare oxide surfaces and supported active metal sites.[20,21]

Formic acid, as the simplest carboxylic acid, is also widely used as a probe molecule for the interaction of carboxylic groups with well-defined catalytic surfaces and has been used to probe acid/base and redox properties[20,22] of surface sites on many oxides, including ZnO,[23−26] MgO,[27−33] TiO_2,[34−44] NiO,[45−47] CeO_2,[48−50] UO_2,[51,52] Fe_3O_4,[53−56] SnO_2,[57] and ZrO_2.[58] Formic acid adsorption on metal oxides can be either molecular or dissociative, depending on the relative acid−base strength of exposed cation−anion pairs. Dissociative adsorption is initiated through the abstraction of an acidic proton by a surface oxygen anion to form a surface hydroxyl. At the same time, the conjugate base (formate, $HCOO^-$) binds to the metal cation. Often, the acid−base properties of these acid−base pairs are defined by the selective formic acid

decomposition through either dehydration ($HCOOH \rightarrow H_2O + CO$, stoichiometric) or dehydrogenation ($HCOOH \rightarrow H_2 + CO_2$, stoichiometric, or $H_2O + CO_2$, nonstoichiometric) pathways.[59,60] These pathways can, therefore, be used to indicate the degree of redox activity of an oxide.

As studied here, formic acid on $Fe_3O_4(001)$ adsorbs at low temperatures (70 K) both dissociatively and molecularly.[53] Experimental and theoretical studies have demonstrated that formate binds by bridging two surface octahedral Fe atoms with the transfer of acidic formic acid hydrogen, forming a lattice-oxygen-bound hydrogen (hydroxyl).[53,54,56,61] However, the complete mechanism for converting formic acid and formate on $Fe_3O_4(001)$ to products has yet to be studied.

In vacuum, the $Fe_3O_4(001)$ surface restructures to form the $(\sqrt{2} \times \sqrt{2})R45°$ reconstruction which is depicted in Figure 1.

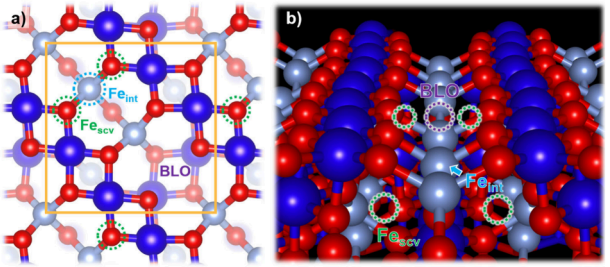

Figure 1. (a) The top-down and (b) the side-on views of the $Fe_3O_4(001)$ surface. Oxygen atoms are displayed as red, Fe octahedral (Fe_{oct}) as blue, and Fe tetrahedral (Fe_{tet}) as gray. The Fe interstitial (Fe_{int}) is circled in light blue, the bulk-like open site (BLO) is labeled in purple, and the subsurface cation Fe vacancies (Fe_{scv}), located beneath surface oxygen atoms, are circled in green. The unit cell is highlighted by a yellow square. A side view of the mirrored slab, Fe oxidation state, and spin orientations is included in the SI, Figure S1.

Here, two subsurface Fe octahedral (Fe_{oct}) atoms migrate to form two subsurface cation vacancies (SCVs). One Fe_{oct} occupies a tetrahedral site at the surface, forming an interstitial Fe (Fe_{int}) atom, while the second Fe atom diffuses into the bulk. Previous experimental work demonstrated the lifting of the SCV reconstruction following the adsorption of atomic hydrogen[62] and formic acid.[53] In these studies, low energy electron diffraction (LEED) showed the disappearance of diffraction spots associated with the presence of Fe_{int}. Subsequent experimental and theoretical studies demonstrated that the Fe_{int} atom and a bulk Fe atom fill the subsurface vacancies and lift the reconstruction when the surface is exposed to formic acid.[54,56]

In this study, we use a combination of X-ray photoelectron spectroscopy (XPS), infrared reflection absorption spectroscopy (IRRAS), temperature-programmed reaction spectroscopy (TPRS), LEED, and density functional theory (DFT) calculations to study formic acid adsorption and reaction on $Fe_3O_4(001)$. We follow the thermal stability of surface intermediates, determine structural changes on the initially reconstructed surface, and identify the reaction products. We find that formic acid primarily decomposes along the dehydration pathway, producing CO through two high-temperature (HT) reaction channels at 530 K (HT1) and 560 K (HT2). The HT2 CO formation channel is also accompanied by minor CO_2 formation (~15%).

We show that hydroxyls play essential roles in the CO formation mechanism. First, via water formation, hydroxyls enable the formation of oxygen vacancies through a Mars-van Krevelen (MvK) mechanism.[53,63−65] Formate species subsequently react with the vacancies, yielding a new type of formate with one of the formate oxygens embedded in the surface lattice. These embedded formate species have a significantly l ower C −H b ond c leavage a nd C O formation barrier. Second, the selectivity toward one of the two CO formation channels depends on surface hydroxyl proximity whereby neighboring hydroxyls facilitate formate decomposition along the lower temperature HT1 CO formation pathway by assisting the C−H cleavage step and stabilizing a bent O−C−O transition state.

2. METHODS

The experiments were conducted in two different ultrahigh vacuum (UHV) systems with base pressures of $<1 \times 10^{-10}$ Torr. The details of the first experimental chamber have been described in previous publications.[66−70] Briefly, t he UHV system is equipped with several instruments, including a quadrupole mass spectrometer (QMS, Hiden), an X-ray source and hemispherical analyzer (Omicron), a quartz crystal microbalance (QCM, Inficon), a nd a l ow e nergy electron diffraction o ptics (LEED, P hysical E lectronics). Sample preparation capabilities include an ion sputter gun (LK Technologies), an auxiliary chamber for producing molecular beams, and a custom hot tungsten−tungsten-filament atomic-hydrogen tube doser.

A natural $10 \times 10 \times 1$ mm^3 $Fe_3O_4(001)$ single crystal (SurfaceNet) is sandwiched between a Ta sample plate and retaining ring. The sample holder assembly is secured together with Mo screws, the tops of which are spot-welded to Ta foil tabs to prevent loosening. A 0.127 mm thick Au foil is compressed between the holder and the back of the crystal to enhance the thermal contact. The sample holder assembly is mounted on a manipulator. The sample can be resistively heated up to 1100 K and cooled to below 60 K via a closed-cycle He cryostat (APD Cryogenics). The temperature was monitored with a K-type thermocouple spot-welded to the back of the sample plate and calibrated via H_2O and CO_2 TPDs. The sample was cleaned through multiple cycles of Ne^+ sputtering (1 kV, Matheson) at a 30° incidence to the sample normal, followed by alternating cycles of annealing at 975 K in UHV and 1×10^{-6} Torr O_2 (Norlab). This procedure is sufficient for restoring the pristine $Fe_3O_4(001)$ $(\sqrt{2} \times \sqrt{2})$ reconstruction and offsets the surface reduction caused by sputtering, noted by the clarity of the LEED pattern and minimization of defect features seen in CO and CO_2 TPDs. Between consecutive TPRS experiments, flashing the sample to 850 K before dosing the surface was sufficient to remove residual adsorbates while retaining the surface reconstruction.

Formic acid and other adsorbate molecules were dosed onto the sample surface via a molecular beam doser of known flux rates calibrated via QCM. The formic acid utilized included regular HCOOH (Alfa Aesar, > 97%) as well as isotopically labeled $H^{13}COOH$ (Cambridge Isotopes, > 98%) and DCOOD (Cambridge Isotopes, > 98%). The formic acid was cleaned before experimentation by repeated freeze−pump−thaw cycles, and a small amount of $CaSO_4$ desiccant pellets (Drierite) was added to the vacuum flasks to remove residual water, which cannot be removed during the freeze−pump−thaw cycles.

The masses monitored during the $H^{13}COOH$ TPRS included m/z = 2 (H_2), 18 (H_2O), 29 (^{13}CO), 30 and 31

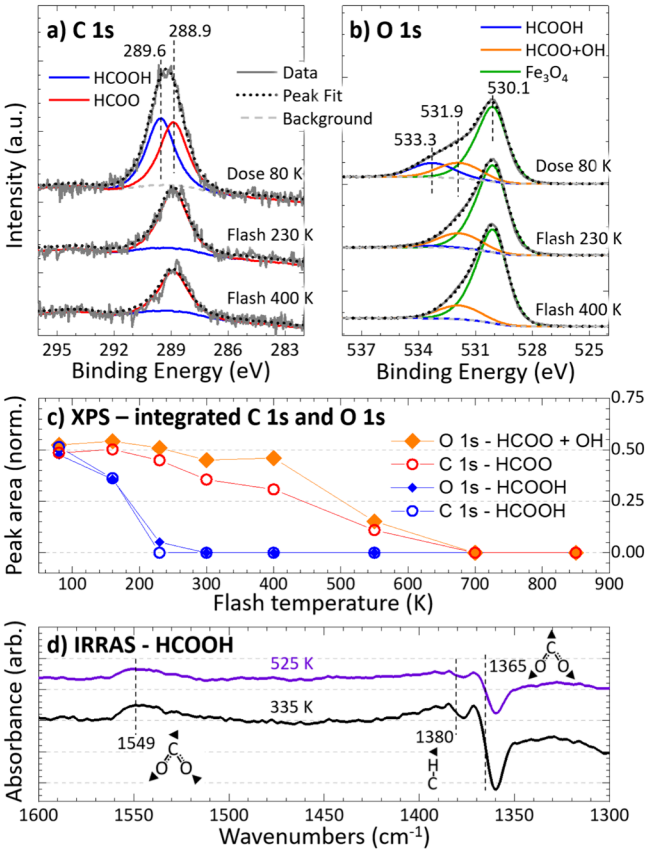

Figure 2. The deprotonation of formic acid on $Fe_3O_4(001)$. (a) C 1s and (b) O 1s XPS data (gray lines) after dosing 5 HCOOH/u.c. on $Fe_3O_4(001)$ at 80 K and ramping to various temperatures at 2 K/s. XPS data were collected at 80 K for ramp temperatures below 300 K and at 300 K for ramp temperatures 300 K and higher. The spectra are fit with two components, one for molecularly bound formic acid (HCOOH, blue) and the other for deprotonated formate (HCOO red and HCOO + OH, orange). $Fe_3O_4(001)$ lattice O 1s fit (b) is shown in green. Panel c shows the integrated peak intensities for HCOOH and HCOO species for both C 1s and O 1s spectra for the full range from 80 to 700 K. The complete set of C 1s and O 1s spectra and the details of the fitting procedure are presented in Figure S2. (d) IRRAS data for 2.7 L of formic acid dosed at 335 K (black) and after ramping to 525 K (purple).

($H_2{}^{13}CO$), 45 ($^{13}CO_2$), and 47 and 48 ($H^{13}COOH$). These masses were appropriately changed when using isotopic $H^{12}COOH$ and $H^{12}COOD$. Each m/z in the TPRS was subtracted by the corresponding m/z in a TPRS blank performed after the initial TPRS to remove background contributions to the signals. To account for the convolution of molecular species contributing to the same monitored m/z channel (e.g., m/z = 28 from CO, CO_2, and HCOOH), cracking patterns of potential products (CO, CO_2, and HCOOH) were obtained by dosing each respective molecule directly into the QMS. The m/z ratios obtained from the cracking patterns were used to deconvolute the TPRS data into signals attributed to individual species. The conversion factors for converting measured signals to molecules·u.c.$^{-1}$s^{-1} desorption rates were calibrated via TPD coverage progression experiments of each respective molecule. The measured CO (from HCOOH) desorption intensity was significantly higher due to the narrowing of the product desorption distribution. A correction factor was determined by comparing the QMS signal of CO from HCOOH and CO from a normal TPRS (sample in-line of the site and normal to the QMS) versus TPRS when the sample is facing away from the QMS. TPRS measurements were collected using a ramp rate of 1 K/s. X-ray photoelectron spectroscopy (XPS) measurements were carried out using Al Kα X-rays with an electron collection angle of 60° relative to the sample normal and an electron pass energy of 50 eV.

The IRRAS measurements were carried out in a second UHV apparatus containing a FTIR spectrometer (Bruker, VERTEX 80v) in a PREVAC UHV system as described in ref.[71] This UHV system is dedicated to IR investigations including both IRRAS at grazing incidence on oxide single crystals and transmission IR measurements on oxide powders.[72−74] IRRAS measurements were conducted at grazing incidence (80°) with a detection limit of $\Delta R/R = \sim 1 \times 10^{-5}$. The base pressure of the measurement chamber is better than 1×10^{-10} mbar and the sample temperature could be varied between ~70 K (cooling by flowing liquid helium) and 1000 K by resistive heating. Formic acid was dosed by backfilling through a leak valve and exposures are given in units of Langmuir (L) (1 L = 1.33×10^{-6} mbar·s).

The DFT calculations were done with the CP2K software package[75] using the PBE exchange-correlation functional[76] augmented with an effective Hubbard U interaction[77] and

norm-conserving pseudopotentials for the core-level electron interactions.[78] The effective Coulomb repulsion parameter for the Fe 3d states of magnetite was set to 4.0 eV, commonly used for $Fe_3O_4(001)$ surface.[62,79,80] This value has been shown to reproduce the structure, band gap, and magnetic moments of bulk magnetite and its surfaces.[3,81,82] Molecularly optimized double-ζ Gaussian MOLOPT basis sets[83] were employed for the Kohn−Sham orbital expansion, with a plane-wave cutoff of 450 Ry for the electrostatics terms. Geometry optimization was performed using the limited memory BFGS method.[84] A symmetric slab model composed of 2 × 2 unit cells in the surface plane and a depth of 8 layers of O and octahedral Fe ions, and 7 layers of tetrahedral Fe ions. The top and bottom layers were $(\sqrt{2} \times \sqrt{2})$ R45° reconstructed based on the Bliem et al. model.[85] The simulation cell includes a 25 Å thick vacuum layer. The unit cell parameters were 17.046 × 17.046 $Å^2$ as obtained from the optimization of a 2 × 2 × 2 bulk Fe_3O_4 super cell (cubic symmetry, a = 17.046 Å). The three outermost layers of O and octahedral Fe ions and two outermost layers of tetrahedral Fe ions were allowed to relax in all calculations with adsorbates. The initial spin states of the Fe atoms were biased toward the high-spin state of their respective oxidation levels based on the Bliem et al.[85] model (±5/2 for Fe^{3+} state and +2 for Fe^{2+}) with the tetrahedral sites antiferromagnetically coupled to the octahedral sites. The resulting total magnetization of the simulation cell is 201. Reducing the spin state of iron results in higher energy configuration. All calculations are done at 3/8 monolayer (ML) coverage, i.e., 0.75 formic acid/u.c., to properly capture the lateral interaction of formic acid adsorbed on Fe_{oct} rows and the reaction of formic acid near the BLO. Because of the 2 × 2 choice of the simulation cell, our calculations sampled four points of the surface Brillouin zone of the unit cell: (0,0), (1/2,0), (0,1/2), and (1/2, 1/2). CP2k does not support the Hubbard U model with explicit multiple *k*-points. We have compared the adsorption energies for different cell sizes and found that it changes negligibly when going from 2 × 2 to 4 × 4 simulations cell sizes.

To determine the lowest energy adsorbate configurations, all geometry optimizations were minimized until the forces fell below 0.001 hartree/Bohr, the lowest energy configuration was further minimized to 0.00045 hartree/Bohr and verified to have no imaginary frequencies. Additionally, the energy and configuration of each minimum were repeated twice, starting from different initial wave functions to verify that the minima were independent of the initial wave function. Minimization for different adsorbate sites and configurations was initiated from the same wave function for faster convergence and consistency. This was done to ensure that adsorbate binding energies are not obfuscated by convergence to different local energetic minima which result from variations in the charge density of Fe within the bulk of the slab. Activation energies were calculated using the climbing-image nudged elastic band method (CI-NEB).[86] The initial and final states of the NEB calculations are optimized as described above. Six images were used between the initial and the final state for all NEB calculations. NEB calculations were minimized until the force was below 0.00045 hartree/Bohr and transition states were confirmed to have only one imaginary frequency. All energies include zero-point energy (ZPE) correction.

3. RESULTS AND DISCUSSION

3.1. The Deprotonation of Adsorbed Formic Acid. We performed temperature-dependent XPS measurements to assess the nature and stability of formic acid-derived surface species adsorbed on $Fe_3O_4(001)$. We dosed 5 HCOOH/u.c. (u.c. = 8.34 Å × 8.34 Å = 69.6 $Å^2$ = 6.96 × 10^{-15} cm^2) onto the reconstructed $Fe_3O_4(001)$ surface at 80 K and ramped the surface (ramp rate 2 K/s) to increasingly higher temperatures (Figure 2 and Figure S2). XPS measurements were taken consecutively after cooling to 80 K (for annealing temperatures up to 300 K) or 300 K (annealing above 300 K) to determine the identity and stability of surface intermediates present during the reactions. Before HCOOH adsorption, C 1s and O 1s spectra were collected on the freshly prepared surface and used as a reference. After the initial formic acid dose, the C 1s spectra (Figure 2a) exhibit a broad peak shape that can be fit with two equivalent Gaussian−Lorentzian peak line shapes centered at 289.6 and 288.9 eV. As observed in previous studies, these peaks correlate well with molecular formic acid (blue) and deprotonated surface-bound formate (red).[53,56] Similarly, the O 1s spectra (Figure 2b) are fit with three Gaussian−Lorentzian product peaks centered at 533.3, 531.9, and 530.1 eV identified previously as molecular formic acid (blue), formate, surface hydroxyls (red), and bulk oxygen of Fe_3O_4 (green), respectively. We note that the peak positions for formate and surface hydroxyls overlap and cannot be decoupled, as demonstrated by the XPS data of hydroxyls prepared by atomic hydrogen deposition as shown in Figure S3.

As the sample is heated to 230 K, the area of the HCOOH-related C 1s and O 1s components drops to zero (Figure 2c, blue) while the area of formate (red) remains constant. This is consistent with the expected initial desorption of more weakly bound molecular formic acid. Ramping to 300 and 400 K leads to a slight coverage decrease (~20%) of the formate species (red), indicating recombinative desorption of formic acid in this temperature range. This is confirmed by TPRS experiments described below in Figure 3. The formate signal drops dramatically after the annealing to 550 K and becomes zero at 700 K. No shifts in binding energy are observed across the entire range of annealing temperatures. The Fe 2p spectra in Figure S2 further indicate a minor reduction of the surface as the formate and hydroxyls are converted to products between 500 and 700 K. The ~711 eV region (Fe(III) cations) decreases slightly, while the ~709 eV region (Fe(II) cations) concomitantly increases.[62,87]

Nonpolarized IRRAS was also performed to assess the evolution of formic acid surface intermediates, Figure 2d and Figure S2d. After dosing 2.7 Langmuir of HCOOH at 335 K (Figure 2d black), peaks appear at 1365, 1380, and 1549 cm^{-1} which are similar to those seen by Gamba et al.[53] The IR bands at 1365 and 1549 cm^{-1} are attributed to the symmetric ν_s(OCO) and asymmetric ν_{as}(OCO) carboxylate stretching vibrations, respectively. Interestingly, the ν_s(OCO) vibration centered at 1365 cm^{-1} exhibits an asymmetric line shape with a maximum at 1371 and a minimum at 1360 cm^{-1}. In earlier work on this system this line shape has been related to a Fano-like behavior originating from a coupling to the conduction electron in this semimetal substrate.[51] We note, however, that this is more likely to result from the so-called polarization-dependent splitting of vibrational modes on semiconductor surfaces.[26,45,46,50,58] The extent of the splitting depends on the

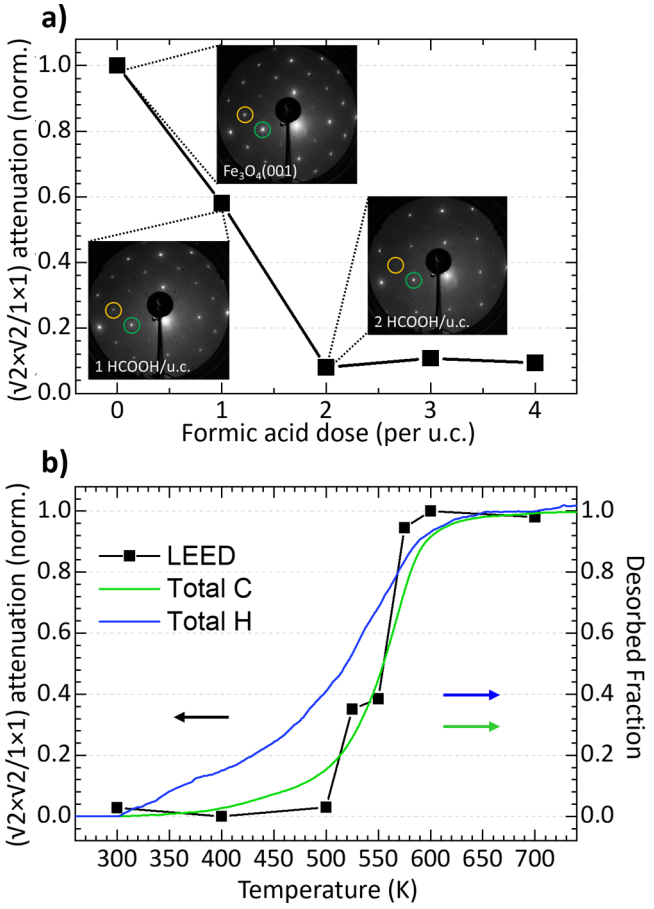

Figure 3. Normalized ratio of $(\sqrt{2} \times \sqrt{2})$ and (1×1) $Fe_3O_4(001)$ LEED spot intensities (black squares) as a function of (a) HCOOH dose at 300 K and (b) annealing temperature for saturation dose of 2 HCOOH/u.c. All data was acquired at 300 K with a beam energy of 66.7 eV, and each image was taken at a different sample location to minimize beam damage. The sample was annealed at the same rate as the TPRS (1 K/s). The yellow and green circles in the LEED images in (a) represent the $(\sqrt{2} \times \sqrt{2})$ and (1×1) LEED spots, respectively. Additional LEED images are displayed in Figures S4 and S5. Green and blue lines in panel (b) are the fractional TPRS product yields of carbon and hydrogen-containing products from 2 HCOOH/u.c. presented in Figure 4.

magnitude of the vibrational transition dipole moment, as analyzed in more detail in previous work.[88] The weak signals at 1380 and 2850 cm^{-1} (Figure S2d) are characteristic of the C−H deformation and stretching vibrations, respectively. The IR features are consistent with those observed for formate species on other oxide surfaces.[26,45,46,50,58] The reversed signs of the ν_s(OCO) and ν_{as}(OCO) bands indicate the formation of bidentate formate with a nearly upright geometry on the $Fe_3O_4(001)$ surface (for a detailed analysis, see ref.72 No vibrational modes associated with ν(C = O) (~1600−1800 cm^{-1}) were observed, demonstrating that no molecular formic acid is present at 335 K.

The 335 K preadsorbed surface was subsequently ramped to 525 K (Figure 2d purple) to monitor changes in intermediate species at desorption temperatures. However, no noticeable changes in peak shape or position were observed, with only a reduction in peak intensity. This indicates that the observed formate intermediate directly leads to the reaction products or if a second intermediate exists, it is short-lived and rapidly converts to reaction products and thus is not observed in the IR spectra.

3.2. The Stability of $Fe_3O_4(001)$ Reconstruction Following Formic Acid Adsorption. We carried out LEED studies to understand structural changes of the $Fe_3O_4(001)$ surface resulting from formic acid adsorption and reaction. Pristine $Fe_3O_4(001)$ exhibits a $(\sqrt{2} \times \sqrt{2})R45°$ LEED pattern due to the formation of the SCV reconstruction and formation of the interstitial Fe (Fe_{int}) as described in Figure 1.[85,89−91] When the reconstruction is lifted, the pattern reverts to a (1×1) periodicity as the Fe_{int} occupies one of the subsurface cation vacancies.[92] Prior results demonstrated that with increasing formic acid and hydroxyl coverages, the bulk terminated surface becomes more thermodynamically stable, filling the subsurface cation vacancies by the Fe_{int} and a bulk Fe atom.[53,54,56,62,63]

Figure 3a shows that the intensity of the $(\sqrt{2} \times \sqrt{2})R45°$ spots decreases linearly as the HCOOH/u.c. coverage is increased to saturation. This is surprising since the critical coverage of hydroxyls required to lift the reconstruction was determined to be 2 H/u.c.,[62] which is only reached at 2 HCOOH/u.c. This may be due to the clustering of the HCOO (and OH) surface species, as indicated by the prior STM results on $Fe_3O_4(001)$.[53] Similar clustering was observed on rutile $TiO_2(110)$ and anatase $TiO_2(101)$ surfaces.[43,93] As such, clustering would create high-density domains where the reconstruction is lifted, even at lower coverages, resulting in an overall linear decrease of the $(\sqrt{2} \times \sqrt{2})R45°$ spot intensities.

Figure 3b (black squares) shows the return of the $(\sqrt{2} \times \sqrt{2})R45°$ reconstruction on the surface covered with 2 HCOOH/u.c., following ramping to different temperatures. The recovery of the normalized $(\sqrt{2} \times \sqrt{2})R45°$ LEED spot intensities (black squares) between 500 and 600 K coincides with the product desorption and restoration of the clean surface. This can be seen from the comparison with the running integrals of the desorbed fraction of hydrogen (blue) and carbon (green) containing species from the identically prepared surface, as seen in Figure 4. As discussed previously, the H-containing products begin to desorb at temperatures 25−50 K lower than those of the C-containing products. Surprisingly, the recovery of the $(\sqrt{2} \times \sqrt{2})$ LEED spots aligns more closely with the desorption of C-containing products than H-containing products.

This finding suggests that surface formate species also hinder the recovery of the $(\sqrt{2} \times \sqrt{2})$ R45° reconstruction. This is further supported by two additional LEED experiments, which show a partial return of the $(\sqrt{2} \times \sqrt{2})$ LEED spot intensities with e^--beam exposure on the HCOOH saturated surface, but no return in spot intensity for an atomic D* dosed surface, as shown in Figure S6. Further, a recent DFT study demonstrated formate stabilization of the bulk-truncated surface and facile diffusion of Fe_{int} into a subsurface cation vacancy.[54]

3.3. The Formation of Reaction Products. The coverage-dependent TPRS spectra collected following $H^{13}COOH$ doses at 120 K on a newly prepared $Fe_3O_4(001)$ sample are shown in Figure 4a. The desorption of unreacted $H^{13}COOH$ and produced ^{13}CO, $^{13}CO_2$, and H_2O is observed with no measurable quantities of H_2 or H_2CO. Analogous $H^{13}COOH$ TPRS spectra obtained on an aged $Fe_3O_4(001)$ used in Rh single-atom experiments[8] exhibit only minor differences, as shown in Figure S7a. The reported absolute formic acid coverages were determined using a flux-calibrated

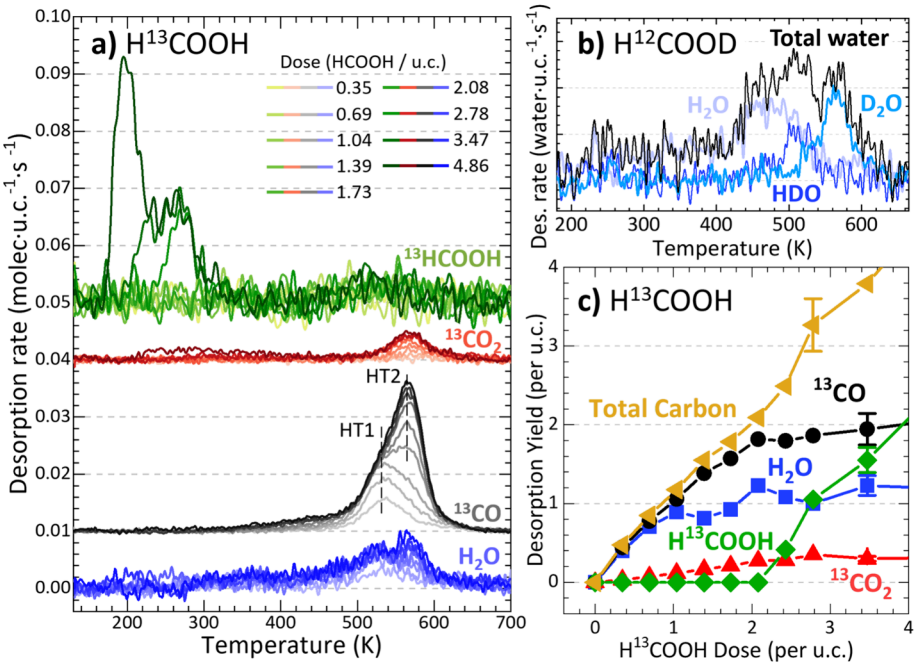

Figure 4. Coverage-dependent TPRS spectra from formic acid ($H^{13}COOH$) adsorbed on $Fe_3O_4(001)$ at 120 K. (a) The desorption spectra of $H^{13}COOH$ reactant and ^{13}CO, $^{13}CO_2$, and H_2O products. Details of the data processing are described in Methods. (b) Water desorption products from a 2.8 $D^{12}COOH$/u.c. TPRS. (c) Integrated desorption yield of the products versus the formic acid dose (via flux-calibrated molecular beam). Integration ranges for the TPRS traces in panel (a) are as follows: H_2O (400−650 K), ^{13}CO (325−650 K), $^{13}CO_2$ (460−650 K), and $H^{13}COOH$ (150−350 K). The error bars were determined by comparison of the integrated C-containing products to dosed $H^{13}COOH$ coverage. The higher doses showing the formation of HCOOH multilayers are shown in Figure S8.

molecular beam and coverage-dependent sticking coefficient measurements. The sticking coefficient measurements were performed using the King and Wells method[94] and determined to be unity within the error of repeat experiments (~3%, data not shown).

3.3.1. Desorption of Formic Acid. The desorption of $H^{13}COOH$ is only observed for coverages above 2 $H^{13}COO$/u.c., which corresponds to the saturation of formate species. This indicates that most formate species undergo further conversion to other products. At higher coverages, two peaks emerge at 190 and 230 K, Figure 4a-top. The peak at 230 K appears first at 2.0−2.5 doses of $H^{13}COOH$/u.c., and is subsequently followed by the development of the peak at 190 K. Since the XPS data (Figure 2c) shows that no molecularly adsorbed formic acid is stable on the surface after heating to 230 K, the 230 K peak likely represents recombinative desorption of bidentate formate with surface hydroxyl. Upon full saturation (~4 $H^{13}COOH$/u.c.), this peak contains ~0.4 $H^{13}COOH$/u.c. The molecular desorption peak at 190 K develops between ~2.5 and 4 HCOOH/u.c. doses where it saturates the peak signal. This peak is followed by the emergence of HCOOH multilayers at higher doses. The formic acid multilayer peak begins to desorb at ~170 K with typical zero-order desorption kinetics (Figure S8). This multilayer peak is easily distinguishable from the monolayer peak as it contains mass fragment 48 (mass 47 is $H^{13}COOH$ parent mass) and is likely a consequence of the desorption of dimerized formic acid molecules.[43,95]

As indicated above, small differences are observed on the aged $Fe_3O_4(001)$ sample (Figure S7, top), where a small amount of formic acid (~0.3 $H^{13}COOH$/u.c.) desorbs between 400 and 600 K. Since only formate is present in the XPS and IRRAS data (Figure 2c,d) above ~230 K, we attribute this feature to the recombinative desorption of formate with hydroxyl hydrogen.

3.3.2. Carbon Monoxide Formation. The primary carbon-containing reaction product is found to be CO (Figure 4a black). The ^{13}CO desorption initially develops as a single broad feature centered between 480 and 600 K that saturates at ~1 $H^{13}COOH$/u.c. As the processes described below are common to ^{13}C labeled and ^{12}C dominated unlabeled formic acid, we omit ^{13}C labeling in the text below. The peak desorption temperature shifts from the initial ~538 K at low coverages (~0.35 HCOOH/u.c.) to 530 K, where it saturates at ~1 HCOOH/u.c. and exhibits an apparent second-order desorption kinetics. We further refer to this feature as the CO HT1 peak. The 530 K feature is followed by the second peak at somewhat higher temperatures (540−600 K), which saturates

at ~2 HCOOH/u.c. and peaks at 560 K (further referred to as CO HT2). In contrast to the CO HT1 peak, the CO HT2 peak has a constant coverage-dependent peak temperature of 560 K and exhibits characteristics of a first-order desorption process. In the 1−2 HCOOH/u.c. coverage range, a broad low-temperature shoulder also populates between 300 and 450 K. A notable difference between the new $Fe_3O_4(001)$ (Figure 4a, black) and aged $Fe_3O_4(001)$ surfaces (Figure S7, black) is an increased CO HT2 yield (~0.4 HCOOH/u.c.) that coincides with a drop in the yield of CO_2 formation and the recombinative desorption of HCOOH. The second difference is the emergence of a high-temperature shoulder at ~650 K for the aged $Fe_3O_4(001)$ (Figure S7, black). These differences likely arise from the increased defect site density (step edges, Fe adatoms, etc.)[96] due to prior metal deposition or extended thermal cycling of the $Fe_3O_4(001)$ single crystal.

3.3.3. Carbon Dioxide Formation. The second minority carbon-containing product observed following the HCOOH exposure is CO_2 (Figure 4a red). CO_2 desorbs as a single peak centered at ~570 K and grows steadily with formate coverages up to 2 HCOOH/u.c. The similar desorption temperature for CO_2 and the HT2 CO desorption peak suggests competing decomposition processes occurring likely on the same reaction sites. Further, the lack of CO_2 formation along the HT1 CO desorption channel indicates that this process significantly differs from the HT2 channel in that it is highly selective to CO formation. At higher doses of formic acid (>2HCOOH/u.c.), broad CO and CO_2 features are observed starting at ~200 K and tailing off at 300 K. As their appearance coincides with the growth of the HCOOH low-temperature desorption peaks, we attribute these features to the reaction of formic acid on hot surfaces of the mass spectrometer ionizer as has been seen in other studies.[39,46]

3.3.4. Water Formation via Mars-van Krevelen Mechanism. The only observed carbon-free desorption product is water (Figure 4a blue). H_2O desorbs over a broad temperature range (~400−650 K), with most water desorbing from a peak initially located at 530 K, reaching a peak maximum at ~2 HCOOH/u.c. The desorption of water in this temperature range is consistent with surface hydroxyl recombination to water via the Mars-van Krevelen mechanism and oxygen vacancy formation.[64,92,97]

To understand the relationship between the initial deprotonation of HCOOH and subsequent C−H bond cleavage leading to CO and CO_2 products, TPRS measurements with $D^{12}COOH$ were performed. The resulting desorption spectra of H_2O, HDO, and D_2O products are shown in Figure 4b. The first water product to desorb is H_2O, which appears at ~400 K, peaks at ~460 K, and ceases at ~550 K. The next product, HDO, desorbs between ~450 and 550 K (peak at ~500 K), and the last product, D_2O, desorbs between 540 and 610 K (peak at ~560 K). The first water species (H_2O) originates from the initial deprotonation of $D^{12}COOH$. The initial HDO shoulder (~470 K) coincides with the HT1 CO desorption shoulder and results from the C−D cleavage step required for CO formation, leaving behind D and O atoms on the surface. The H_2O and HDO traces simultaneously recede around 530 K, indicating a decrease in OH coverage through water desorption. As formate decomposition to CO proceeds along the HT1 CO channel, new surface OD species are formed, and D_2O desorption increases while H_2O and HDO desorption decrease. The D_2O desorption parallels the transition from the HT1 CO to the HT2 CO channel.

3.3.5. Formic Acid Reaction Mechanism from TPRS. Total product yields obtained by integrating the TPRS traces in Figure 4a as a function of formic acid dose are shown in Figure 4c. Generally, up to a saturation coverage of 2 $H^{13}COOH$/u.c., all product yields (^{13}CO, $^{13}CO_2$, H_2O) increase monotonically and approximately linear with increasing dose. Above this coverage, the desorption of reaction products plateaus, and only the low-temperature $H^{13}COOH$ desorption continues to increase linearly. This shows that all formic acid directly bound on Fe_{oct} sites[53−56] as bidentate formate and hydroxyls are converted to the reaction products.

On the new sample, these are only CO and CO_2, while on the aged sample, a small amount (<15%) desorbs recombinatively as $H^{13}COOH$ (see Figure S7). The desorption product yields in Figure 4c demonstrate that carbon desorbing in carbon-containing products equals the carbon dosed as formic acid. CO dominates the distribution and accounts for ~70−87% of desorbing carbon. Both CO_2 and HCOOH account for ~12−30%.

A somewhat worse agreement is obtained for H-containing products (H_2O and HCOOH), where the yield of desorbing hydrogen accounts only for ~50% of that expected based on the formic acid (FA) dose (Figure 4c blue and green). The origin of this discrepancy may be due to the difficulty of collecting a small and broad water desorption signal. A similar discrepancy has also been reported on other metal oxides.[29,49,57,98] The TPRS data in Figure 4 shows that the selective HCOOH decomposition on the $Fe_3O_4(001)$ surface heavily favors the dehydration pathway, producing approximately 4.5−6 times more CO than CO_2, depending on sample age and surface defect concentration.

The coverage-dependence of CO TPRS spectra (Figure 4c black) with two maxima that are filling in from the lower-temperature HT1 peak (~530 K) at low coverages (0−1 FA/u.c.) to the higher-temperature HT2 peak (~560 K) at high coverages (1−2 FA/u.c.) is puzzling. At low coverage, the lower-temperature regime demonstrates the availability of a lower energy HT1 reaction pathway not utilized by all adsorbed formate species when the starting coverages are high. Several factors can contribute to the two-channel dehydration mechanism. The early concurrent desorption of H_2O and CO indicates that hydroxyls may play an important role in differentiating these two CO pathways. The formation of oxygen vacancies via water formation could yield different formate species (e.g., via the reaction of bidentate formate with the oxygen vacancy). Additionally, the differences in the activity of the Fe_{oct} binding sites (e.g., with or without the OH neighbors) can be important. Further, $Fe_3O_4(001)$ reconstruction is lifted upon formic acid adsorption and subsequently reformed by 623 K,[62] introducing another possibility that surface restructuring also plays an important role in directing low/high channels and CO versus CO_2 formation. Further experiments designed to test these suppositions are discussed in the following sections.

3.4. The Effect of Surface Hydroxyls on the Kinetics of Formate Conversion to CO. To test whether the two CO reaction channels (TPRS peaks HT1 and HT2 in Figure 4) result from the formate being immobilized and reacting on two different sites, we carried out experiments using isotopically labeled HCOOH species. Figure 5a shows ^{13}CO (blue) and $^{13}CO_2$ (purple) TPRS reference spectra following 2 $H^{13}COOH$/u.c. adsorption (analogous to those shown in Figure 4a).

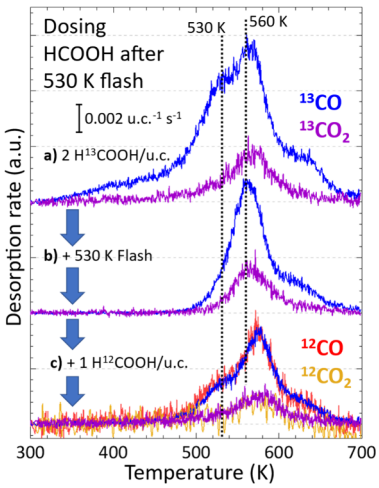

Figure 5. Set of CO (blue and red) and CO_2 (purple and orange) TPRS experiments following the dose of isotopically labeled HCOOH at 300 K. (a) TPRS after 2 $H^{13}COOH$/u.c. dose. (b) TPRS after 2 $H^{13}COOH$/u.c. dose, ramp to 530 K, and cooling to 300 K. (c) TPRS after 2 $H^{13}COOH$/u.c. dose, ramp to 530 K, cooling to 300 K, and 1 $H^{12}COOH$/u.c. dose. The TPRS spectra are offset to illustrate changes resulting from each preparation step. Vertical dashed lines at 530 and 560 K are added to highlight the CO reaction channels HT1 and HT2, respectively.

Figure 5b, shows TPRS spectra following the adsorption of 2 $H^{13}COOH$/u.c., ramping to 530 K, and subsequently cooling to 300 K. The resulting TPRS (Figure 5b) only exhibits the HT2 ^{13}CO (blue) peak at 560 K and $^{13}CO_2$ (purple) peak at 570 K. This experiment demonstrates that the C-containing surface-intermediate/active-site configuration that yields ^{13}CO product via HT1 peak cannot be regenerated from the remaining C-containing surface intermediates (~1 intermediate/u.c.). It should be noted that the surface with the remaining formate that desorbs via HT2 is practically free of hydroxyl species produced by formic acid deprotonation as they desorbed as water at lower temperatures within the HT1 region (see Figure 4b).

To assess whether the lack of the conversion of remaining formate via HT1 is a result of the limited mobility, we took the surface prepared in Figure 5b (~1 HCOO/u.c. is still on the surface) and dosed a second isotope 1 $H^{12}COOH$/u.c. The resulting TPRS in Figure 5c shows a complete mixing of ^{12}C and ^{13}C HCOOH isotopes. This demonstrates that the first-dosed isotope (here ^{13}C) can be completely redistributed and desorbed via the HT1 TPRS channel with the same probability as the ^{12}C isotope. This redistribution excludes the possibility that the 530 K annealing has induced the formation of a new surface intermediate which is less reactive than the one being converted via the HT1 channel. A separate TPRS experiment involving the subsequent dose of 1 $H^{13}COOH$/u.c. and 1 HCOOH/u.c. (without annealing between the doses) also shows a complete mixing of the formate species (see Figure S9).

We considered two possibilities:

(1) High local HCOO coverage is required to enable the low-temperature conversion via HT1, possibly via lifting of the reconstruction, as shown in Figure 3a. This supposition would be consistent with the clustering of the formate species observed in a prior STM study,[96] but inconsistent with the annealing-dependent recovery of the reconstruction on formic acid-covered surfaces shown in Figure 3b. There, annealing to 530 K does not lift the reconstruction completely, indicating the presence of some high-density domains despite the absence of CO formation via the HT1 channel.

(2) The presence of surface hydroxyl species is critical for the HT1 reaction channel. The initially high coverage of hydroxyls was achieved by the deprotonation of 2 HCOOH/u.c. leads to 2 OH/u.c. surface coverage. This coverage has been shown to lift the surface reconstruction[62] However, as already discussed in (1), the reconstruction alone cannot be the reason for the presence of two observed HT1 and HT2 channels. The TPRS experiments with DCOOH having isotopically labeled hydrogen positions (Figure 4b), demonstrate that all water derived from surface hydroxyls (OH) originates from formic acid deprotonation (H) and desorbs by 530−550 K. Therefore, any hydroxyls that form via C−D bond cleavage at higher temperatures will recombine immediately as they are not limited by slow kinetics of water formation. Therefore, TPRS features HT1 as operating in the abundance of surface hydroxyl species while HT2 operates mostly in their absence.

To determine whether surface hydroxyls affect fractioning into HT1 and HT2 CO formation pathways, TPRS spectra were taken after increasing the surface hydroxyl coverage by dosing atomic hydrogen. The same preparation procedure was adopted, which led to the TPRS spectra shown in Figure 5b. The reference TPRS from 2 $H^{13}COOH$/u.c. is shown in Figure 6a. Figure 6b, shows the TPRS from the surface prepared as in Figure 6a after ramping to 530 K and cooling to 300 K. The surface prepared as in Figure 6b is then modified by dosing a 50% saturation dose of atomic D, as calibrated with LEED and XPS and detailed in Figure S3. The resulting TPRS, Figure 6c, shows that the leading edge and peak of the CO

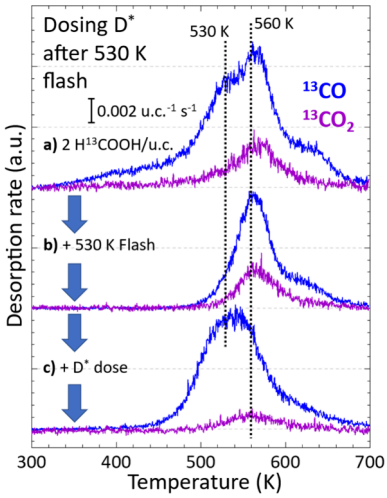

Figure 6. 2 $H^{13}COOH$/u.c. TPRS highlighting the effects of rehydrogenation after ramping to 530 K. (a) 2 $H^{13}COOH$/u.c. dosed at 300 K. (b) After ramping the surface to 530 K. (c) After dosing a 530 K ramped surface with 50% of the saturation coverage of atomic hydrogen. The TPRS spectra have not been calibrated to a desorption rate as in Figure 2 due to uncertainty in how the atomic hydrogen dosing affects the angular desorption of the CO product. Vertical dashed lines at 530 and 560 K are added to highlight the CO reaction channels HT1 and HT2, respectively.

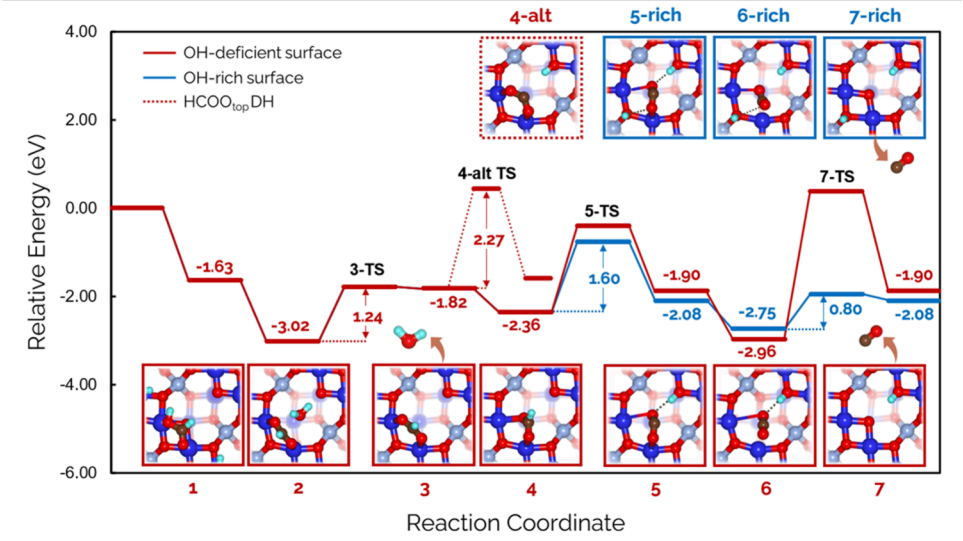

Figure 7. Energy diagram of HCOOH decomposition to CO on hydroxyl-deficient (red) and hydroxyl-rich (blue) $(\sqrt{2} \times \sqrt{2})$R45° reconstructed Fe_3O_4 (001). All energies are corrected with ZPE and referenced to a clean reconstructed Fe_3O_4 (001) surface and three noninteracting gas-phase formic acid molecules. Inserts of the minima configurations for the hydroxyl-deficient paths are framed in red, and the hydroxyl-rich surface is shown in blue (labeled as 5, 6, 7-rich). A dotted red line shows a direct C−H bond cleavage of the bidentate formate step (4-alt). The Fe_{oct}, Fe_{tet}, C, O, and H atoms are represented as blue, light blue-gray, brown, red, and teal spheres. The hydroxyl-deficient/rich surfaces refer to the location of the OH relative to the BLO. The number of H present is consistent for all calculations. Additional molecular figures highlighting the oxygens from the reactant are included in the SI (Figure S15).

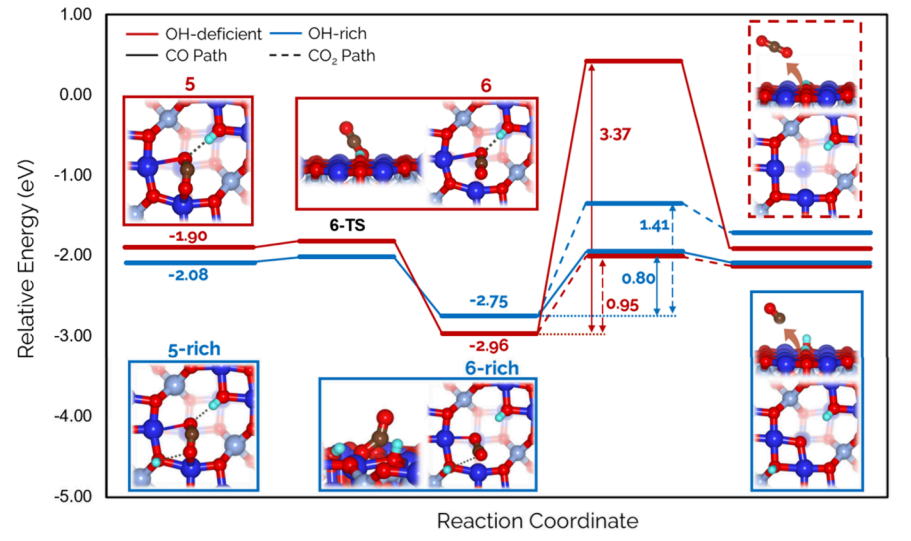

Figure 8. The comparison of different pathways yielding OCO configurations (steps 5 and 6 in Figure 7) on the $(\sqrt{2} \times \sqrt{2})$R45° reconstructed Fe_3O_4 (001) surface. The energies are referenced to a clean surface with three noninteracting gaseous formic acid molecules. The differences in the final states are due to the differences in energy of the OH-deficient and OH-rich surfaces. The Fe_{oct}, Fe_{tet}, C, O, and H atoms are represented as blue, light blue-gray, brown, red, and teal spheres, respectively. Energies are references to the final state of step 5 (embedded OCO). From step 6 on both surfaces, the CO production pathway energetics are denoted with a solid line, and the CO_2 production pathway energetics are denoted with a dashed line.

desorption have downshifted considerably to the temperature range of the HT1 reaction channel. Further, the area of CO desorbing from the surface increased by 54%, while CO_2 decreased by 58% compared to the hydroxyl-free TPRS (Figure 6b).

3.5. Formic Acid Decomposition Mechanisms Based on DFT Calculations. DFT calculations were used to investigate the possible effects of surface conditions on the reaction pathways for CO and CO_2 formation, i.e. oxygen vacancy (O_{vac}) formation, the proximity of hydroxyl to the reacting formate, and the lifting of the surface reconstruction.

3.5.1. Mars-van Krevelen Mediated Water and Oxygen Vacancy Formation. The energetics of the proposed reaction mechanism of HCOOH decomposition to CO on reconstructed Fe_3O_4 (001) at 3/8 ML formic acid coverage is shown in Figure 7. This coverage is selected to account for the lateral interactions between the adsorbates during the reaction (for adsorbate configurations and interactions, see Section 10 of the

supplement and Figures S10 and S11). Adsorption of three HCOOH molecules on reconstructed Fe_3O_4 (001) (step 1, Figure 7) is downhill (exoergic) in energy by 1.63 eV, corresponding to the adsorption energy of 0.54 eV per HCOOH molecule, in agreement with previous results on other metal oxides.[47,99] The deprotonation of HCOOH to formate and hydroxyl, followed by the formation of surface-bound water with the second surface hydroxyl near the BLO (step 2, Figure 7), is further downhill by 1.39 eV. The subsequent desorption of water via the MvK mechanism requires 1.24 eV and leads to the formation of O_{vac} (steps 3-TS and 3, Figure 7). The favorability of O_{vac} formation at the BLO (versus other oxygens) is discussed further in Section 11 of the supplement and Figures S12 and S13. The estimate of the energetics of water formation from TPRS (Figure 4b) using the first-order desorption kinetics, prefactor of 10^{13} s^{-1}, and the observed water desorption rate of 0.002 H_2O/u.c./s at ~400 K yields a desorption energy of ~1.1 eV,[100] consistent with our TPRS spectra.

The subsequent C−H bond cleavage of the formate shown in step 3 is very high (~2.27 eV, step 4-alt TS, Figure 7) and, therefore, unlikely. In contrast with this high barrier pathway, the formation of O_{vac} enables a distinct reaction pathway where one of the formate oxygens fills the $O_{vac,}$ forming a formate embedded in the surface (step 4, Figure 7). The C−H bond cleavage of this embedded formate is significantly easier, as discussed in the next section.

3.5.2. The Influence of Hydroxyl Species on CO and CO_2 Formation. To understand the experimentally observed effect of surface hydroxyls on the formation of CO and CO_2, we carried out calculations with hydroxyl-deficient (red) and hydroxyl-rich (blue) surfaces for the reaction steps following the formation of embedded formate (steps 5−7, Figure 7, Figure S14, and Table S1). Hydroxyl-deficient and hydroxyl-rich refers to the amount of OH near the BLO but the total number of OH are kept consistent for the deficient and rich calculations. The reaction pathway for the hydroxyl-rich surface (shown in blue and figure inserts labeled 5-, 6-, and 7-rich) is represented by a slab with the OH bound to two Fe_{oct} at the BLO and across from the embedded formate. The addition of OH near the embedded HCOO lowers the activation barrier for the C−H bond cleavage (step 5-TS, Figure 7) from 1.96 eV on the hydroxyl-deficient surface to 1.60 eV on the hydroxyl-rich surface. More importantly, it affects the subsequent barrier of C−O bond scission (step 7-TS, Figure 7), which is necessary to form CO. The nearby OH decreases this barrier from 3.37 eV (step 7-TS, red) to 0.80 eV (step 7-TS, blue).

The effects of the OH are shown on Figure 8 which depicts the reaction and activation energies for CO and CO_2 formation with and without hydroxyl. On the hydroxyl-rich surface, a bent (activated) OCO configuration is stabilized after the formate C−H bond cleavage through the interactions with the OH (step 6-rich, Figure 8). In contrast, a deactivated, linear OCO configuration forms on the hydrogen-deficient surface (step 6, Figure 8). The reaction path from the bent configuration (hydroxyl-rich) has a lower activation barrier to release CO (blue solid line, 0.80 eV) than CO_2 (blue dashed line, 1.41 eV). In contrast, for the linear OCO configuration (hydroxyl-deficient), the CO_2 formation (red dashed line, 0.95 eV) is more favorable than C−O bond cleavage and CO formation (red solid line, 3.37 eV). This may explain why, experimentally, CO_2 is primarily observed on the hydroxyl-deficient surface.

A proximal OH stabilizes the bent OCO configuration via hydrogen bonding, and the subsequent C−O bond-breaking step becomes more facile, favoring CO production. Mulliken charge analysis indicates that hydroxyls reduce the charges of neighboring Fe_{oct} atoms. The decrease in the oxidation state of the Fe_{oct} strengthens the interaction between the Fe_{oct} and OCO, which inhibits CO_2 desorption and favors C−O bond scission to CO.

3.5.3. The Influence of Lifting of the Fe_3O_4(001) Reconstruction on Reaction Kinetics. The LEED images of Figure 3a suggest that the decomposition of HCOO may occur on a surface where the reconstruction is lifted, which can affect the decomposition pathway. The structure of a slab where the reconstruction is locally lifted is described in the SI (Figure S11), and the energetics of HCOOH decomposition on this locally lifted surface are shown in Figure S16. Overall, the pathway for HCOOH decomposition to CO at low OH coverage on the locally lifted surface (Figure S16, OH-deficient) shares similar mechanistic behavior as that on the reconstructed surface for reaction steps at low OH coverage (Figure 7, OH-deficient). However, with high OH coverage (Figure S16, OH-rich), very little change is observed compared to the OH-deficient surface. This result contrasts with what was observed for the reconstructed surface, where a hydroxyl-rich surface significantly reduced the barrier for the C−O cleavage step and CO formation (Figure 7, OH-rich). The stabilization effect of the hydroxyls on the embedded OCO intermediate for this locally lifted surface is minimal, mainly due to the orientation of the hydroxyl near the interstitial vacancy (Figure S17, panels D), which is oriented toward the vacancy (created when the Fe_{int} diffuses to a SCV). This inhibits interaction with the OCO intermediate, leading to the formation of a linear OCO despite the presence of OH. As a result, adding hydroxyl on the locally lifted surface does not show any significant effects on the energetics pathway, and the production of CO is not favored, as observed on the reconstructed surface.

As mentioned earlier, in the TPRS and LEED data (Figure 4 and Figure 3) taken during the formic acid adsorption and reaction, the recovery of the $(\sqrt{2} \times \sqrt{2})R45°$ pattern coincides more closely with the desorption of CO or CO_2 rather than H_2O desorption. This suggests that the return of the $(\sqrt{2} \times \sqrt{2})R45°$ reconstruction occurs after the vacancy formation by water desorption and subsequent embedment of HCOO into the vacancy. The increase in Fe_{oct}−O bond length of the embedded formate on the locally lifted surface (2.25 Å, lower-right panel Figure S18) compared to the bidentate formate (2.01 Å, upper-middle panel Figure S18) suggests weaker interactions. This weakening in the chemisorption of embedded formate may induce recovery of the local reconstruction, i.e., the return of sublayer Fe_{oct} to the Fe_{int} position.[53,54,56,62,91] The reformation of Fe_{int} at 500−600 K is very facile due to the low energy barrier of 0.05 eV for the diffusion of Fe_{oct} from the sublayer into the interstitial site.[54] Based on this, we speculate that the lifting of the reconstruction is reversed after the surface vacancy formation and embedment of HCOO into the surface. The reappearance of the Fe_{int} reintroduces the effect of OH near the reactive site, where the OCO is stabilized in a bent configuration, favoring CO production.

3.6. Summary of the Reaction Mechanism. The behavior of formic acid on the $Fe_3O_4(001)$ is surprisingly complex. This is a consequence of the structural changes that occur during the formic acid adsorption and subsequent product formation. Below, we summarize the above-discussed structural factors that include lifting of the surface reconstruction, presence of the surface hydroxyls, and formation of the oxygen vacancies on the observed catalytic chemistry, and the two CO formation channels (HT1 and HT2).

3.6.1. Formation of Bidentate Formate Species. The deprotonation of formic acid is well established, supported by our XPS, IRRAS, and DFT results in Figure 2 and Figure 7. Since there are no shifts in C 1s and O 1s XPS peak positions and no changes in the observed IR frequencies along the TPRS ramp, bidentate formate is found to be the only stable, long-lived intermediate before product formation.

The LEED results presented in Figure 4 further show that upon formic acid deprotonation at 300 K, the total area of the surface that is reconstructed decreases linearly with increasing coverage. This linear decrease suggests the presence of unreconstructed regions (at least several nm in size) that become larger as the coverage increases. This finding is consistent with the previous LEED and STM study.[53] Further, the studies of H atom adsorption[62] concluded that hydroxyl coverage of 2H/u.c. is required to lift the surface reconstruction. This surface hydroxyl coverage can only be reached if formic acid clusters on the surface. Furthermore, STM studies at lower than saturation coverages (2 formic acid/u.c.) suggested clustering of the formate species.[53]

3.6.2. Water Formation via the Mars-van Krevelen Mechanism. The fact that water desorption in TPRS precedes CO desorption indicates that lattice oxygen participates in the water formation process. Past studies of formic acid on metal oxide surfaces have stressed the importance of hydroxyl recombination to water and oxygen vacancy formation in CO formation.[29,35,36,39,41,43,48,49,58,101] Here, two adjacent hydroxyls react to form water. The fact that the water desorption precedes the formation of carbon-containing products, as shown in Figure 4b (blue line), clearly indicates that oxygen is being abstracted from the lattice, creating an oxygen vacancy.

3.6.3. The Thermal Stability of Bidentate Formate Intermediate. The findings presented in Figure 2 argue against forming a second stable formate species that would form along the TPRS ramp. In particular, we expect the bidentate formate to react with oxygen vacancies above ~400 K due to recombinative water formation from surface hydroxyls.[64,92,97] Our DFT results (Figure 7) demonstrate that such a barrierless reaction creates a surface-embedded formate, with one formate oxygen integrated into the surface and coordinating with three iron atoms. Studies on other oxides have demonstrated the importance of oxygen vacancies in the formate decomposition pathway to CO.[29,35,36,39,41,43,48,49,58,101] The minimum energy pathway under hydroxyl-rich conditions (HT1) suggests the embedded formate is stable, with subsequent C−H cleavage being the rate-limiting step (Figure 7). The lack of this embedded formate species observed in IRRAS indicates this species exists as a minority and, after its formation, quickly reacts to CO or CO_2.

3.6.4. Recovery of the Surface Reconstruction during Product Formation. The LEED results in Figure 3b show that the $Fe_3O_4(001)$ reconstruction reforms as the reaction products desorb during the TPRS ramp (500−600 K). The reappearance of the reconstruction correlates more closely with the annealing-induced CO product formation rather than H_2O formation. This suggests that formate species stabilize the lifting of the reconstruction, similar to the presence of surface hydroxyls. Our DFT work demonstrates that energy barriers are prohibitively high for the C−O bond cleavage step to release CO on the locally lifted surface (even when it is hydroxyl-rich) compared to the reconstructed surface. The Fe_{int} on the reconstructed surface promotes hydroxyl interaction with the OCO intermediate, reducing the barrier toward CO formation. The continued yield of CO then indicates that at some point along this reaction pathway, the reconstruction is locally restored. In agreement, the TPRS and LEED data (Figure 3 and 4) shows the recovery of the $(\sqrt{2} \times \sqrt{2})R45°$ pattern coincides more closely with the desorption of CO or CO_2 rather than H_2O desorption.

3.6.5. Surface Hydroxyls and Two Reaction Channels in CO Formation. The presence and absence of surface hydroxyls during the HT1 and HT2 CO desorption (Figure 4a), respectively, are the only evident characteristics that we could identify as a distinguishing factor for these two desorption channels. The liberation of formate trapped in the HT2 channel after atomic hydrogen adsorption, Figure 6, provides compelling evidence that hydroxyls present during the decomposition to CO lower the energy barrier for the rate-limiting step, resulting in the HT1 desorption peak.

DFT calculations suggest that an adjacent surface hydroxyl promotes CO production by stabilizing an OCO bent configuration through hydrogen bonding to the hydroxyl. Furthermore, hydroxyls reduce the neighboring Fe_{oct} atom, increasing the Fe_{oct}−O interaction and stabilizing the OCO bent configuration. Additionally, the OCO−OH and Fe_{oct}−O interactions weaken the OCO interaction with the OH across the BLO, preventing rearrangement to a linear OCO configuration. These effects promote the production of CO on the hydroxyl-rich surface observed in the HT1 channel.

3.6.6. CO_2 Formation. The desorption temperature range of CO_2 peak within TPRS coincides with that of HT2 CO, suggesting a common surface intermediate (Figure 4). Our DFT calculations indicate that CO_2 can react along two pathways through a bidentate or embedded bidentate intermediate. The bidentate pathway has a steep barrier to CO_2 formation, making it unlikely (Figure 7). Under hydroxyl-deficient conditions, the conversion of embedded formate is favored due to its lower reaction barrier (Figure 8). Under the hydroxyl-rich conditions of the HT1 channel, CO_2 formation is inaccessible, making CO the only carbon-containing product. Under the HT2 hydroxyl-deficient regime, the lack of hydroxyls favors CO_2 formation. However, the formation of surface hydroxyls, which causes formate to react along the CO pathway preferentially, limits the overall CO_2 production. This is consistent with the TPRS data, where the CO to CO_2 yield is 4:1 within the HT2 channel.

4. CONCLUSIONS

Our mechanistic studies of the formic acid reactions on the reconstructed $Fe_3O_4(001)$ surface reveal how the dynamic changes in the surface structure and the level of hydroxylation of the oxide surface during the reaction affect the reaction pathways. We have shown that the reaction proceeds at low temperatures via formic acid deprotonation on the pristine oxide, yielding formate and hydroxyl species adsorbed on the

surface. Two reaction channels are observed for the carbon-containing products at 530 and 560 K. The 530 K channel only shows the formation of CO, which closely follows water production via the Mars-van Krevelen mediated mechanism. Theoretical calculations show that the bidentate formate readily reacts with the resulting oxygen vacancy to yield a new formate species with one of its oxygens embedded in the surface. The 560 K channel yields both CO and CO_2 products. The lower activation barrier of the first reaction channel is facilitated by the presence of hydroxyls that originate from the deprotonation of the formic acid. DFT calculations show that hydroxyls stabilize the bent OCO intermediate, leading to preferential CO formation. The lack of hydroxyls in the 560 K channel yields a linear OCO intermediate, which leads to CO_2 formation. Since hydroxyls are also created during the C−H bond cleavage in the 560 K channel, CO is also produced.

Our findings demonstrate the importance of hydroxyls in influencing the reaction barriers and selective promotion of reaction products on oxide surfaces. Ultimately, these results illustrate the dynamic nature of the iron-oxide surface during the reaction and demonstrate how changes in the concentration of surface intermediates, such as hydroxyls, heavily influence surface activity and reaction kinetics.

AUTHOR INFORMATION

Corresponding Authors

Simone Raugei − *Physical and Computational Sciences Directorate and Institute for Integrated Catalysis, Pacific Northwest National Laboratory, Richland, Washington 99354, United States;* orcid.org/0000-0001-9118-8480; Email: simone.raugei@pnnl.gov

Líney Árnadóttir − *Physical and Computational Sciences Directorate and Institute for Integrated Catalysis, Pacific Northwest National Laboratory, Richland, Washington 99354, United States; School of Chemical, Bioengineering, and Environmental Engineering, Oregon State University, Corvallis, Oregon 97330, United States;* orcid.org/0000-0001-9013-4173; Email: liney.arnadottir@oregonstate.edu

Zdenek Dohnálek − *Physical and Computational Sciences Directorate and Institute for Integrated Catalysis, Pacific Northwest National Laboratory, Richland, Washington 99354, United States; Voiland School of Chemical Engineering and Bioengineering, Washington State University, Pullman, Washington 99163, United States;* orcid.org/0000-0002-5999-7867; Email: zdenek.dohnalek@pnnl.gov

Authors

Marcus A. Sharp − *Physical and Computational Sciences Directorate and Institute for Integrated Catalysis, Pacific Northwest National Laboratory, Richland, Washington 99354, United States; Voiland School of Chemical Engineering and Bioengineering, Washington State University, Pullman, Washington 99163, United States;* orcid.org/0000-0002-2599-8212

Hoan K. K. Nguyen − *School of Chemical, Bioengineering, and Environmental Engineering, Oregon State University, Corvallis, Oregon 97330, United States;* orcid.org/0000-0003-1797-9860

Christopher J. Lee − *Physical and Computational Sciences Directorate and Institute for Integrated Catalysis, Pacific Northwest National Laboratory, Richland, Washington 99354, United States;* orcid.org/0000-0002-8703-8209

Eric Sauter − *Institute of Functional Interfaces (IFG), Karlsruhe Institute of Technology (KIT), 76344 Eggenstein-Leopoldshafen, Germany*

Yuemin Wang − *Institute of Functional Interfaces (IFG), Karlsruhe Institute of Technology (KIT), 76344 Eggenstein-Leopoldshafen, Germany;* orcid.org/0000-0002-9963-5473

Christof Wöll − *Institute of Functional Interfaces (IFG), Karlsruhe Institute of Technology (KIT), 76344 Eggenstein-Leopoldshafen, Germany;* orcid.org/0000-0003-1078-3304

Benjamin A. Jackson − *Physical and Computational Sciences Directorate and Institute for Integrated Catalysis, Pacific Northwest National Laboratory, Richland, Washington 99354, United States;* orcid.org/0000-0001-6205-8951

Mal-Soon Lee − *Physical and Computational Sciences Directorate and Institute for Integrated Catalysis, Pacific Northwest National Laboratory, Richland, Washington 99354, United States;* orcid.org/0000-0001-6851-177X

Bruce D. Kay − *Physical and Computational Sciences Directorate and Institute for Integrated Catalysis, Pacific Northwest National Laboratory, Richland, Washington 99354, United States;* orcid.org/0000-0002-8543-2341

Notes

The authors declare no competing financial interest.

ACKNOWLEDGMENTS

This work was supported by the U.S. Department of Energy, Office of Science, Basic Energy Sciences, Chemical Sciences, Geosciences, and Biosciences Division, Catalysis Science Program, FWP 47319. PNNL is a multiprogram national laboratory operated for DOE by Battelle under Contract DE-AC05-76RL01830. E.S., Y.W., and C.W. acknowledge the Deutsche Forschungsgemeinschaft (DFG, German Research

Foundation) – Project-ID 426888090 – SFB 1441 (projects A4 and B3).

REFERENCES

(1) Novotny, Z.; Argentero, G.; Wang, Z.; Schmid, M.; Diebold, U.; Parkinson, G. S. Ordered array of single adatoms with remarkable thermal stability: Au/Fe_3O_4(001). *Phys. Rev. Lett.* **2012**, *108* (21), 216103.

(2) Rossell, M. D.; Caparrós, F. J.; Angurell, I.; Muller, G.; Llorca, J.; Seco, M.; Rossell, O. Magnetite-supported palladium single-atoms do not catalyse the hydrogenation of alkenes but small clusters do. *Catal. Sci. Technol.* **2016**, *6* (12), 4081–4085.

(3) Meier, M.; Jakub, Z.; Balajka, J.; Hulva, J.; Bliem, R.; Thakur, P. K.; Lee, T. L.; Franchini, C.; Schmid, M.; Diebold, U.; et al. Probing the geometry of copper and silver adatoms on magnetite: quantitative experiment versus theory. *Nanoscale* **2018**, *10* (5), 2226–2230.

(4) Yuk, S. F.; Collinge, G.; Nguyen, M. T.; Lee, M. S.; Glezakou, V. A.; Rousseau, R. Selective acetylene hydrogenation over single metal atoms supported on Fe_3O_4(001): A first-principle study. *J. Chem. Phys.* **2020**, *152* (15), 154703.

(5) Jakub, Z.; Hulva, J.; Ryan, P. T. P.; Duncan, D. A.; Payne, D. J.; Bliem, R.; Ulreich, M.; Hofegger, P.; Kraushofer, F.; Meier, M.; et al. Adsorbate-induced structural evolution changes the mechanism of CO oxidation on a Rh/Fe_3O_4(001) model catalyst. *Nanoscale* **2020**, *12* (10), 5866–5875.

(6) Hulva, J.; Meier, M.; Bliem, R.; Jakub, Z.; Kraushofer, F.; Schmid, M.; Diebold, U.; Franchini, C.; Parkinson, G. S. Unraveling CO adsorption on model single-atom catalysts. *Science* **2021**, *371* (6527), 375–379.

(7) Kraushofer, F.; Parkinson, G. S. Single-atom catalysis: Insights from model systems. *Chem. Rev.* **2022**, *122* (18), 14911–14939.

(8) Sharp, M. A.; Lee, C. J.; Mahapatra, M.; Smith, R. S.; Kay, B. D.; Dohnálek, Z. Preparation and characterization of model homotopic catalysts: Rh adatoms, nanoparticles, and mixed oxide surfaces on Fe_3O_4(001). *J. Phys. Chem. C* **2022**, *126* (34), 14448–14459.

(9) Bliem, R.; Pavelec, J.; Gamba, O.; McDermott, E.; Wang, Z.; Gerhold, S.; Wagner, M.; Osiecki, J.; Schulte, K.; Schmid, M.; et al. Adsorption and incorporation of transition metals at the magnetite Fe_3O_4(001) surface. *Phys. Rev. B* **2015**, *92* (7), 075440.

(10) Ratnasamy, C.; Wagner, J. P. Water gas shift catalysis. *Catal. Rev. - Sci. Eng.* **2009**, *51* (3), 325–440.

(11) Huang, L.; Han, B.; Zhang, Q.; Fan, M.; Cheng, H. Mechanistic study on water gas shift reaction on the Fe_3O_4(111) reconstructed surface. *J. Phys. Chem. C* **2015**, *119* (52), 28934–28945.

(12) Zhu, M.; Wachs, I. E. Iron-based catalysts for the high-temperature water-gas shift (HT-WGS) reaction: A review. *ACS Catal.* **2016**, *6* (2), 722–732.

(13) Huff, G. A.; Satterfield, C. N. Intrinsic kinetics of the Fischer–Tropsch synthesis on a reduced fused-magnetite catalyst. *Ind. Eng. Chem. Proc. Design Devel.* **1984**, *23* (4), 696–705.

(14) Dictor, R. Fischer–Tropsch synthesis over reduced and unreduced iron oxide catalysts. *J. Catal.* **1986**, *97* (1), 121–136.

(15) Satterfield, C. N.; Hanlon, R. T.; Tung, S. E.; Zou, Z. M.; Papaefthymiou, G. C. Initial behavior of a reduced fused-magnetite catalyst in the Fischer–Tropsch synthesis. *Ind. Eng. Chem. Prod. Res. Dev.* **1986**, *25* (3), 401–407.

(16) Rao, K. R. P. M.; Huggins, F. E.; Mahajan, V.; Huffman, G. P.; Rao, V. U. S. The role of magnetite in Fischer–Tropsch synthesis. *Hyperfine Interact.* **1994**, *93* (1), 1745–1749.

(17) Khan, M. M. T.; Halligudi, S. B.; Shukla, S. Reduction of CO_2 by molecular hydrogen to formic acid and formaldehyde and their decomposition to CO and H_2O. *J. Mol. Catal.* **1989**, *57* (1), 47–60.

(18) Leitner, W. Carbon dioxide as a raw material: The synthesis of formic acid and its derivatives from CO_2. *Angew. Chem., Int. Ed. Engl.* **1995**, *34* (20), 2207–2221.

(19) Nelson, N. C.; Nguyen, M.-T.; Glezakou, V.-A.; Rousseau, R.; Szanyi, J. Carboxyl intermediate formation via an in situ-generated metastable active site during water-gas shift catalysis. *Nat. Catal.* **2019**, *2* (10), 916–924.

(20) Vohs, J. M. Site requirements for the adsorption and reaction of oxygenates on metal oxide surfaces. *Chem. Rev.* **2013**, *113* (6), 4136–4163.

(21) Diebold, U. The surface science of titanium dioxide. *Surf. Sci. Rep.* **2003**, *48* (5–8), 53–229.

(22) Barteau, M. A. Site requirements of reactions on oxide surfaces. *J. Vac. Sci. Technol., A* **1993**, *11* (4), 2162–2168.

(23) Crook, S.; Dhariwal, H.; Thornton, G. HREELS study of the interaction of formic acid with ZnO($10\bar{1}0$) and ZnO($000\bar{1}$)-O. *Surf. Sci.* **1997**, *382* (1–3), 19–25.

(24) Vohs, J. M.; Barteau, M. A. Conversion of methanol, formaldehyde and formic acid on the polar faces of zinc oxide. *Surf. Sci.* **1986**, *176* (1–2), 91–114.

(25) Petrie, W. T.; Vohs, J. M. An HREELS investigation of the adsorption and reaction of formic acid on the (0001)-Zn surface of ZnO. *Surf. Sci.* **1991**, *245* (3), 315–323.

(26) Buchholz, M.; Li, Q.; Noei, H.; Nefedov, A.; Wang, Y.; Muhler, M.; Fink, K.; Wöll, C. The interaction of formic acid with zinc oxide: A combined experimental and theoretical study on single crystal and powder samples. *Top. Catal.* **2015**, *58* (2–3), 174–183.

(27) Petrie, W. T.; Vohs, J. M. Application of HREEL spectroscopy to characterize adsorbates on insulating metal oxide surfaces: carboxylates on MgO(100). *Surf. Sci. Lett.* **1991**, *259* (3), L750–L756.

(28) Domen, K.; Akamatsu, N.; Yamamoto, H.; Wada, A.; Hirose, C. Infrared-visible sum frequency generation study of HCOOH on an MgO(001) surface. *Surf. Sci.* **1993**, *283* (1–3), 468–472.

(29) Yamamoto, H.; Watanabe, N.; Wada, A.; Domen, K.; Hirose, C. Adsorption and decomposition of formic acid on MgO(001) surface as investigated by temperature programmed desorption and sum-frequency generation spectroscopy: Recurrence induced defect sites. *J. Chem. Phys.* **1997**, *106* (11), 4734–4744.

(30) Wu, M.-C.; Goodman, D. W. Acid/base properties of MgO studied by high resolution electron energy loss spectroscopy. *Catal. Lett.* **1992**, *15* (1–2), 1–11.

(31) Peng, X. D.; Barteau, M. A. Spectroscopic characterization of surface species derived from HCOOH, CH_3COOH, CH_3OH, C_2H_5OH, $HCOOCH_3$, and C_2H_2 on MgO thin film surfaces. *Surf. Sci.* **1989**, *224* (1–3), 327–347.

(32) Peng, X. D.; Barteau, M. A. Dehydration of carboxylic acids on the MgO(100) surface. *Catal. Lett.* **1991**, *7* (5–6), 395–402.

(33) Peng, X. D.; Barteau, M. A. Acid-base properties of model MgO surfaces. *Langmuir* **1991**, *7* (7), 1426–1431.

(34) Bowker, M.; Stone, P.; Bennett, R.; Perkins, N. Formic acid adsorption and decomposition on TiO_2(110) and on Pd/TiO_2(110) model catalysts. *Surf. Sci.* **2002**, *511* (1–3), 435–448.

(35) Hayden, B. E.; King, A.; Newton, M. A. Fourier transform reflection-absorption IR spectroscopy study of formate adsorption on TiO_2(110). *J. Phys. Chem. B* **1999**, *103* (1), 203–208.

(36) Henderson, M. A. Complexity in the decomposition of formic acid on the TiO_2(110) surface. *J. Phys. Chem. B* **1997**, *101* (2), 221–229.

(37) Idriss, H. Surface reactions of uranium oxide powder, thin films and single crystals. *Surf. Sci. Rep.* **2010**, *65* (3), 67–109.

(38) Onishi, H.; Aruga, T.; Iwasawa, Y. Switchover of reaction paths in the catalytic decomposition of formic acid on TiO_2(110) surface. *J. Catal.* **1994**, *146* (2), 557–567.

(39) Petrik, N. G.; Wang, Y.; Wen, B.; Wu, Y.; Ma, R.; Dahal, A.; Gao, F.; Rousseau, R.; Wang, Y.; Kimmel, G. A.; et al. Conversion of formic acid on single- and nano-crystalline anatase TiO_2(101). *J. Phys. Chem. C* **2021**, *125* (14), 7686–7700.

(40) Tanner, R. E.; Liang, Y.; Altman, E. I. Structure and chemical reactivity of adsorbed carboxylic acids on anatase TiO_2(001). *Surf. Sci.* **2002**, *506* (3), 251–271.

(41) Uemura, Y.; Taniike, T.; Tada, M.; Morikawa, Y.; Iwasawa, Y. Switchover of reaction mechanism for the catalytic decomposition of HCOOH on a TiO_2(110) surface. *J. Phys. Chem. C* **2007**, *111* (44), 16379–16386.

(42) Wang, L. Q.; Ferris, K. F.; Shultz, A. N.; Baer, D. R.; Engelhard, M. H. Interactions of HCOOH with stoichiometric and defective TiO_2(110) surfaces. *Surf. Sci.* **1997**, *380* (2−3), 352−364.
(43) Wang, Y.; Wen, B.; Dahal, A.; Kimmel, G. A.; Rousseau, R.; Selloni, A.; Petrik, N. G.; Dohnalek, Z. Binding of formic acid on anatase TiO_2(101). *J. Phys. Chem. C* **2020**, *124*, 20228−20239.
(44) Xu, M.; Noei, H.; Buchholz, M.; Muhler, M.; Wöll, C.; Wang, Y. Dissociation of formic acid on anatase TiO_2(101) probed by vibrational spectroscopy. *Catal. Today* **2012**, *182* (1), 12−15.
(45) Truong, C. M.; Wu, M. C.; Goodman, D. W. Adsorption and reaction of formic acid on NiO(100) films on Mo(100): Temperature programmed desorption and high resolution electron energy loss spectroscopy studies. *J. Chem. Phys.* **1992**, *97* (12), 9447−9453.
(46) Xu, C.; Goodman, D. W. Surface chemistry of polar oxide surfaces: Formic acid on NiO(111). *J. Chem. Soc., Faraday Trans.* **1995**, *91* (20), 3709.
(47) Zhao, W.; Doyle, A. D.; Morgan, S. E.; Bajdich, M.; Nørskov, J. K.; Campbell, C. T. Formic acid dissociative adsorption on NiO(111): Energetics and structure of adsorbed formate. *J. Phys. Chem. C* **2017**, *121* (50), 28001−28006.
(48) Gordon, W. O.; Xu, Y.; Mullins, D. R.; Overbury, S. H. Temperature evolution of structure and bonding of formic acid and formate on fully oxidized and highly reduced CeO_2(111). *Phys. Chem. Chem. Phys.* **2009**, *11* (47), 11171−11183.
(49) Senanayake, S. D.; Mullins, D. R. Redox pathways for HCOOH decomposition over CeO_2 surfaces. *J. Phys. Chem. C* **2008**, *112* (26), 9744−9752.
(50) Stubenrauch, J.; Brosha, E.; Vohs, J. M. Reaction of carboxylic acids on CeO_2(111) and CeO_2(100). *Catal. Today* **1996**, *28* (4), 431−441.
(51) Chong, S. V.; Idriss, H. Reactions of acetic acid on UO_2(111) single crystal surfaces. *J. Vac. Sci. Technol., A* **2000**, *18* (4), 1900−1905.
(52) Chong, S. V.; Idriss, H. The reactions of carboxylic acids on UO_2(111) single crystal surfaces. Effect of gas-phase acidity and surface defects. *Surf. Sci.* **2002**, *504*, 145−158.
(53) Gamba, O.; Noei, H.; Pavelec, J.; Bliem, R.; Schmid, M.; Diebold, U.; Stierle, A.; Parkinson, G. S. Adsorption of formic acid on the Fe_3O_4(001) surface. *J. Phys. Chem. C* **2015**, *119* (35), 20459−20465.
(54) Arndt, B.; Sellschopp, K.; Creutzburg, M.; Grånäs, E.; Krausert, K.; Vonk, V.; Müller, S.; Noei, H.; Feldbauer, G. B. V.; Stierle, A. Carboxylic acid induced near-surface restructuring of a magnetite surface. *Commun. Chem.* **2019**, *2* (1), 92.
(55) Creutzburg, M.; Sellschopp, K.; Tober, S.; Granas, E.; Vonk, V.; Mayr-Schmolzer, W.; Muller, S.; Noei, H.; Vonbun-Feldbauer, G. B.; Stierle, A. Heterogeneous adsorption and local ordering of formate on a magnetite surface. *J. Phys. Chem. Lett.* **2021**, *12* (15), 3847−3852.
(56) Ryan, P. T. P.; Payne, D. J.; Lee, T. L.; Duncan, D. A. Quantitative structure determination of adsorbed formate and surface hydroxyls on Fe_3O_4(001). *Phys. Chem. Chem. Phys.* **2021**, *24* (1), 488−496.
(57) Gercher, V. A.; Cox, D. F. Formic acid decomposition on SnO_2(110). *Surf. Sci.* **1994**, *312* (1−2), 106−114.
(58) Dilara, P. A.; Vohs, J. M. TPD and HREELS investigation of the reaction of formic acid on zirconium dioxide (100). *J. Phys. Chem.* **1993**, *97* (49), 12919−12923.
(59) Ruelle, P.; Kesselring, U. W.; Nam-Tran, H. Ab initio quantum-chemical study of the unimolecular pyrolysis mechanisms of formic acid. *J. Am. Chem. Soc.* **1986**, *108* (3), 371−375.
(60) Saito, K.; Shiose, T.; Takahashi, O.; Hidaka, Y.; Aiba, F.; Tabayashi, K. Unimolecular decomposition of formic acid in the gas phase-on the ratio of the competing reaction channels. *J. Phys. Chem. A* **2005**, *109* (24), 5352−5357.
(61) Bianchetti, E.; Di Valentin, C. Effect of surface functionalization on the magnetization of Fe_3O_4 nanoparticles by hybrid density functional theory calculations. *J. Phys. Chem. Lett.* **2022**, *13* (40), 9348−9354.
(62) Parkinson, G. S.; Mulakaluri, N.; Losovyj, Y.; Jacobson, P.; Pentcheva, R.; Diebold, U. Semiconductor-half metal transition at the Fe_3O_4(001) surface upon hydrogen adsorption. *Phys. Rev. B* **2010**, *82* (12), 125413.
(63) Doudin, N.; Yuk, S. F.; Marcinkowski, M. D.; Nguyen, M.-T.; Liu, J.-C.; Wang, Y.; Novotny, Z.; Kay, B. D.; Li, J.; Glezakou, V. A.; et al. Understanding heterolytic H_2 cleavage and water-assisted hydrogen spillover on Fe_3O_4(001)-supported single palladium atoms. *ACS Catal.* **2019**, *9* (9), 7876−7887.
(64) Parkinson, G. S.; Novotny, Z.; Jacobson, P.; Schmid, M.; Diebold, U. Room temperature water splitting at the surface of magnetite. *J. Am. Chem. Soc.* **2011**, *133* (32), 12650−12655.
(65) Mars, P.; van Krevelen, D. W. Oxidations carried out by means of vanadium oxide catalysts. *Chem. Eng. Sci.* **1954**, *3*, 41−59.
(66) Lee, C. J.; Sharp, M. A.; Smith, R. S.; Kay, B. D.; Dohnálek, Z. Adsorption of ethane, ethene, and ethyne on reconstructed Fe_3O_4(001). *Surf. Sci.* **2021**, *714*, 121932.
(67) Marcinkowski, M. D.; Adamsen, K. C.; Doudin, N.; Sharp, M. A.; Smith, R. S.; Wang, Y.; Wendt, S.; Lauritsen, J. V.; Parkinson, G. S.; Kay, B. D.; et al. Adsorption and reaction of methanol on Fe_3O_4(001). *J. Chem. Phys.* **2020**, *152* (6), 064703.
(68) Tait, S. L.; Dohnalek, Z.; Campbell, C. T.; Kay, B. D. n-alkanes on MgO(100). I. Coverage-dependent desorption kinetics of n-butane. *J. Chem. Phys.* **2005**, *122* (16), 164707.
(69) Tait, S. L.; Dohnalek, Z.; Campbell, C. T.; Kay, B. D. n-alkanes on MgO(100). II. Chain length dependence of kinetic desorption parameters for small n-alkanes. *J. Chem. Phys.* **2005**, *122* (16), 164708.
(70) Dohnalek, Z.; Kim, J.; Bondarchuk, O.; White, J. M.; Kay, B. D. Physisorption of N_2, O_2, and CO on fully oxidized TiO_2(110). *J. Phys. Chem. B* **2006**, *110* (12), 6229−6235.
(71) Wang, Y.; Glenz, A.; Muhler, M.; Wöll, C. A new dual-purpose ultrahigh vacuum infrared spectroscopy apparatus optimized for grazing-incidence reflection as well as for transmission geometries. *Rev. Sci. Instrum.* **2009**, *80* (11), 113108.
(72) Wang, Y.; Wöll, C. IR spectroscopic investigations of chemical and photochemical reactions on metal oxides: bridging the materials gap. *Chem. Soc. Rev.* **2017**, *46* (7), 1875−1932.
(73) Yang, C.; Wöll, C. Infrared Reflection-Absorption Spectroscopy (IRRAS) applied to oxides: Ceria as a case study. *Surf. Sci.* **2024**, *749*, 122550.
(74) Yang, C.; Idriss, H.; Wang, Y.; Woll, C. Surface structure and chemistry of CeO_2 powder catalysts determined by surface-ligand infrared spectroscopy (SLIR). *Acc. Chem. Res.* **2024**, *57* (22), 3316−3326.
(75) VandeVondele, J.; Krack, M.; Mohamed, F.; Parrinello, M.; Chassaing, T.; Hutter, J. Quickstep: Fast and accurate density functional calculations using a mixed Gaussian and plane waves approach. *Comput. Phys. Commun.* **2005**, *167* (2), 103−128.
(76) Perdew, J. P.; Burke, K.; Ernzerhof, M. Generalized gradient approximation made simple. *Phys. Rev. Lett.* **1996**, *77* (18), 3865−3868.
(77) Dudarev, S. L.; Botton, G. A.; Savrasov, S. Y.; Humphreys, C. J.; Sutton, A. P. Electron-energy-loss spectra and the structural stability of nickel oxide: An LSDA+U study. *Phys. Rev. B* **1998**, *57* (3), 1505−1509.
(78) Goedecker, S.; Teter, M.; Hutter, J. Separable dual-space Gaussian pseudopotentials. *Phys. Rev. B Condens.* **1996**, *54* (3), 1703−1710.
(79) Jeng, H. T.; Guo, G. Y.; Huang, D. J. Charge-orbital ordering and Verwey transition in magnetite. *Phys. Rev. Lett.* **2004**, *93* (15), 156403.
(80) Leonov, I.; Yaresko, A. N.; Antonov, V. N.; Korotin, M. A.; Anisimov, V. I. Charge and orbital order in Fe_3O_4. *Phys. Rev. Lett.* **2004**, *93* (14), 146404.
(81) Noh, J.; Osman, O. I.; Aziz, S. G.; Winget, P.; Bredas, J. L. A density functional theory investigation of the electronic structure and spin moments of magnetite. *Sci. Technol. Adv. Mater.* **2014**, *15* (4), 044202.

(82) Yu, X.; Huo, C.-F.; Li, Y.-W.; Wang, J.; Jiao, H. Fe_3O_4 surface electronic structures and stability from GGA+U. *Surf. Sci.* **2012**, *606* (9−10), 872−879.
(83) VandeVondele, J.; Hutter, J. Gaussian basis sets for accurate calculations on molecular systems in gas and condensed phases. *J. Chem. Phys.* **2007**, *127* (11), 114105.
(84) Nocedal, J. Updating quasi-Newton matrices with limited storage. *Math. Comput.* **1980**, *35* (151), 773−782.
(85) Bliem, R.; McDermott, E.; Ferstl, P.; Setvin, M.; Gamba, O.; Pavelec, J.; Schneider, M. A.; Schmid, M.; Diebold, U.; Blaha, P.; et al. Subsurface cation vacancy stabilization of the magnetite (001) surface. *Science* **2014**, *346* (6214), 1215−1218.
(86) Henkelman, G.; Uberuaga, B. P.; Jónsson, H. A climbing image nudged elastic band method for finding saddle points and minimum energy paths. *J. Chem. Phys.* **2000**, *113* (22), 9901−9904.
(87) Descostes, M.; Mercier, F.; Thromat, N.; Beaucaire, C.; Gautier-Soyer, M. Use of XPS in the determination of chemical environment and oxidation state of iron and sulfur samples: constitution of a data basis in binding energies for Fe and S reference compounds and applications to the evidence of surface species of an oxidized pyrite in a carbonate medium. *Appl. Surf. Sci.* **2000**, *165* (4), 288−302.
(88) Zerulla, B.; Krstic, M.; Chen, S.; Yu, Z.; Beutel, D.; Holzer, C.; Nyman, M.; Nefedov, A.; Wang, Y.; Mayerhofer, T. G.; et al. Polarization-dependent effects in vibrational absorption spectra of 2D finite-size adsorbate islands on dielectric substrates. *Phys. Chem. Chem. Phys.* **2024**, *26* (18), 13683−13693 From NLM PubMed-not-MEDLINE.
(89) Arndt, B.; Bliem, R.; Gamba, O.; van der Hoeven, J. E. S.; Noei, H.; Diebold, U.; Parkinson, G. S.; Stierle, A. Atomic structure and stability of magnetite Fe_3O_4(001): An X-ray view. *Surf. Sci.* **2016**, *653*, 76−81.
(90) Fonin, M.; Pentcheva, R.; Dedkov, Y. S.; Sperlich, M.; Vyalikh, D. V.; Scheffler, M.; Rüdiger, U.; Güntherodt, G. Surface electronic structure of the Fe_3O_4(100): Evidence of a half-metal to metal transition. *Phys. Rev. B* **2005**, *72* (10), 104436.
(91) Parkinson, G. S.; Novotný, Z.; Jacobson, P.; Schmid, M.; Diebold, U. A metastable Fe(A) termination at the Fe_3O_4(001) surface. *Surf. Sci.* **2011**, *605* (15−16), L42−L45.
(92) Parkinson, G. S. Iron oxide surfaces. *Surf. Sci. Rep.* **2016**, *71* (1), 272−365.
(93) Ma, R.; O'Connor, C. R.; Collinge, G.; Allec, S. I.; Lee, M. S.; Dohnalek, Z. The role of surface hydroxyls in the mobility of carboxylates on surfaces: Dynamics of acetate on anatase TiO_2(101). *J. Phys. Chem. Lett.* **2023**, *14* (10), 2542−2550.
(94) King, D. A.; Wells, M. G. Molecular beam investigation of adsorption kinetics on bulk metal targets: Nitrogen on tungsten. *Surf. Sci.* **1972**, *29* (2), 454−482.
(95) Chao, J.; Zwolinski, B. J. Ideal gas thermodynamic properties of methanoic and ethanoic acids. *J. Phys. Chem. Ref. Data* **1978**, *7* (1), 363−377.
(96) Gamba, O.; Hulva, J.; Pavelec, J.; Bliem, R.; Schmid, M.; Diebold, U.; Parkinson, G. S. The role of surface defects in the adsorption of methanol on Fe_3O_4(001). *Top. Catal.* **2017**, *60* (6−7), 420−430.
(97) Bliem, R.; van der Hoeven, J.; Zavodny, A.; Gamba, O.; Pavelec, J.; de Jongh, P. E.; Schmid, M.; Diebold, U.; Parkinson, G. S. An atomic-scale view of CO and H_2 oxidation on a Pt/Fe_3O_4 model catalyst. *Angew. Chem., Int. Ed.* **2015**, *54* (47), 13999−14002.
(98) Idriss, H.; Lusvardi, V. S.; Barteau, M. A. Two routes to formaldehyde from formic acid on TiO_2(001) surfaces. *Surf. Sci.* **1996**, *348* (1−2), 39−48.
(99) Ludviksson, A.; Zhang, R.; Campbell, C. T.; Griffiths, K. The chemisorption and reactions of formic acid on Cu films on ZnO (000)-O. *Surf. Sci.* **1994**, *313* (1−2), 64−82.
(100) Redhead, P. A. Thermal desorption of gases. *Vacuum* **1962**, *12* (4), 203−211.
(101) Kinoshita, K.; Suzuki, S.; Chun, W.-J.; Takakusagi, S.; Asakura, K. Adsorption structure of acetic anhydride on a TiO_2(110) surface observed by scanning tunneling microscopy. *Surf. Sci.* **2009**, *603* (3), 552−557.